Supplementary Materials for

Generation of extreme-ultraviolet beams with time-varying orbital angular momentum

Laura Rego*†, Kevin M. Dorney*†, Nathan J. Brooks, Quynh L. Nguyen, Chen-Ting Liao, Julio San Román, David E. Couch, Allison Liu, Emilio Pisanty, Maciej Lewenstein, Luis Plaja, Henry C. Kapteyn, Margaret M. Murnane, Carlos Hernández-García

*Corresponding author. Email: laura.rego@usal.es (L.R.); kevin.dorney@colorado.edu (K.M.D.)
†These authors contributed equally to this work.

Published 28 June 2019, *Science* **364**, eaaw9486 (2019)
DOI: 10.1126/science.aaw9486

This PDF file includes:

Other Supplementary Materials for this manuscript include the following:
(available at science.sciencemag.org/content/364/6447/eaaw9486/suppl/DC1)

Supplementary Text

S1. Derivation of the Theoretical Equation for the Self-Torque of Light

The physical nature of the self-torque imprinted into extreme-ultraviolet (EUV) beams can be understood through the conservation of orbital angular momentum (OAM) during the high-order harmonic generation (HHG) process. To begin, we consider HHG driven by two time-delayed linearly polarized infrared (IR) vortices with different OAM, ℓ_1 and ℓ_2, such that $|\ell_1 - \ell_2|$=1. In order to extract the OAM contributions, we follow a similar derivation as performed in the Supplementary Information of (*20*). In contrast to the analysis performed in (*20*), in this work the weight of the two drivers is not the same, but instead varies in time.

Let us consider the total driving field as the superposition of two OAM pulses with complex amplitudes $U_1(\rho, \phi, t)$ and $U_2(\rho, \phi, t)$, expressed in cylindrical coordinates (ρ, ϕ, z). For non-zero angular momenta, these fields have a ring-shaped amplitude profile. We consider the beams such that the rings of maximal intensity overlap (i.e., those of the same radius) in the gas target, located at the focus position (z=0). Since the harmonic conversion efficiency is optimal along the intensity ring, we describe the total amplitude in the radius of maximal intensity as

$$U(\phi, t) = U_1(t)e^{i\ell_1\phi} + U_2(t)e^{i\ell_2\phi} \qquad \text{[S1]}.$$

Defining $U_0(t) = U_1(t) + U_2(t)$, the relative amplitude for the second driving pulse is given by $\eta(t) = U_2(t)/U_0(t)$, therefore we can write the resulting field at the target as

$$U(\phi, t) = U_0(t)\left[(1-\eta)e^{i\ell_1\phi} + \eta e^{i\ell_2\phi}\right] = U_0(t)e^{i(\ell_1+\ell_2)\phi/2}\left[\cos\frac{(\ell_1-\ell_2)\phi}{2} + i\big(1-2\eta(t)\big)\sin\frac{(\ell_1-\ell_2)\phi}{2}\right] \text{[S2]}.$$

For simplicity in notation, we will drop the time variable in the following derivations. We can factorize $U(\phi) = |U(\phi)|e^{i\,\varphi(\phi)}$, where the intensity and phase are given by,

$$|U(\phi)|^2 = |U_0|^2\left\{[1-2\eta]^2 + 4\eta[1-\eta]\,\cos^2\left[\frac{(\ell_1-\ell_2)\phi}{2}\right]\right\} \qquad \text{[S3]}$$

$$\varphi(\phi) = \arctan\left\{[1-2\eta]\tan\frac{(\ell_1-\ell_2)\phi}{2}\right\} + \frac{(\ell_1+\ell_2)}{2}\phi \qquad \text{[S4]}.$$

The phase term can be approximated by

$$\varphi(\phi) \approx [1-2\eta]\frac{(\ell_1-\ell_2)}{2}\phi + \frac{(\ell_1+\ell_2)}{2}\phi = \{[1-\eta]\ell_1 + \eta\ell_2\}\phi \qquad \text{[S5]}.$$

In order to calculate the q^{th}-order harmonic field we follow the Strong Field Approximation (SFA) model (*57, 72*), where the q^{th}-order harmonic amplitude scales with the amplitude of the driver with an exponent $p<q$ (we take $p=4$ for the plateau harmonics, driven in argon by 800 nm laser pulses, as shown in the Supplemental Information of (*20*)). On the other hand, the phase of the q^{th}-order harmonic corresponds to q times the phase of the driving field, plus the intrinsic phase (*57, 72*). Neglecting the

latter—as it gives rise to secondary OAM contributions of nearly an order of magnitude weaker (*18*)—the q^{th}-order harmonic amplitude, $A_q(\phi)$, can be written as

$$A_q(\phi) \propto |U(\phi)|^p e^{iq\varphi(\rho,\phi)} = \left[|U(\phi)|e^{i\varphi(\phi)}\right]^p e^{i(q-p)\varphi(\phi)} = U^p(\phi)e^{i(q-p)\varphi(\phi)} \quad \text{[S6]}.$$

Inserting the form of the driving field given by Eq. S2, we arrive at the following,

$$\begin{aligned} A_q(\phi) &\propto U_0^p\left[(1-\eta)e^{i\ell_1\phi} + \eta e^{i\ell_2\phi}\right]^p e^{i(q-p)\varphi(\phi)} \\ &= U_0^p\left[\sum_{r=0}^{p}\binom{p}{r}(1-\eta)^r e^{ir\ell_1\phi}\ \eta^{(p-r)}e^{i(p-r)\ell_2\phi}\right]e^{i(q-p)\varphi(\phi)} \end{aligned} \quad \text{[S7]},$$

where r is an integer. Finally, using Eq. S5 and writing explicitly the temporal dependence, the q^{th}-order harmonic is given by

$$\begin{aligned} A_q(\phi,t) \propto U_0^p(t)&\left[\sum_{r=0}^{p}\binom{p}{r}\left(1-\bar{\eta}(t)\right)^r e^{ir\ell_1\phi}\ \bar{\eta}^{(p-r)}(t)e^{i(p-r)\ell_2\phi}\right] \\ &\times e^{i(q-p)[(1-\eta(t))\ell_1+\eta(t)\ell_2]\phi} \end{aligned} \quad \text{[S8]},$$

where $\bar{\eta}(t)$ is the average of $\eta(t)$ over the half cycle that contributes to a particular harmonic. On the right side of Eq. S8 we can identify two terms that contain azimuthally dependent phase terms, and thus contribute to the OAM content: the sum over *r*, and the last exponential term. This latter term has an explicit OAM contribution while the OAM of the sum over *r* is more involved.

Each term in the sum over *r* in Eq. S8 has a definite angular momentum $r\ell_1 + (p-r)\ell_2$. Therefore, the sum corresponds to the combination of these angular momentum contributions according to a binomial statistical distribution with probabilities $P_{\ell_1} = 1-\bar{\eta}(t)$ and $P_{\ell_2} = \bar{\eta}(t)$. The mean angular momentum of the sum over *r*, thus, corresponds to

$$\begin{aligned} \langle \ell_q(t)\rangle = \sum_{r=0}^{p}\binom{p}{r}P_{\ell_1}^r P_{\ell_2}^{(p-r)}[r\ell_1 + (p-r)\ell_2] = (\ell_1-\ell_2)\sum_{r=0}^{p}\binom{p}{r}P_{\ell_1}^r P_{\ell_2}^{(p-r)}r + \\ p\ell_2\sum_{r=0}^{p}\binom{p}{r}P_{\ell_1}^r P_{\ell_2}^{(p-r)} \end{aligned} \quad \text{[S9]}.$$

Taking into account that $\sum_{r=0}^{p}\binom{p}{r}P_{\ell_1}^r P_{\ell_2}^{(p-r)} = 1$, and that $\sum_{r=0}^{p}\binom{p}{r}P_{\ell_1}^r P_{\ell_2}^{(p-r)}r = pP_{\ell_1}$, we can extract the mean OAM of this sum as

$$\langle \ell_q(t)\rangle = \sum_{r=0}^{p}\binom{p}{r}P_{\ell_1}^r P_{\ell_2}^{(p-r)}[r\ell_1 + (p-r)\ell_2] = p\{[1-\bar{\eta}(t)]\ell_1 + \bar{\eta}(t)\ell_2\} \quad \text{[S10]}$$

As a consequence, from Eq. S8, the mean OAM of the q^{th} harmonic is given by

$$\begin{aligned} \bar{\ell}_q(t) &= \langle \ell_q(t)\rangle + (q-p)\{[1-\bar{\eta}(t)]\ell_1 + \bar{\eta}(t)\ell_2\} \\ &= q[(1-\bar{\eta}(t))\ell_1 + \bar{\eta}(t)\ell_2] \end{aligned} \quad \text{[S11]}.$$

The width of the OAM distribution at each instant of time can be calculated as

$$\sigma_{\ell_q} = \sqrt{\langle \ell_q^2(t) \rangle - \left[\langle \ell_q(t) \rangle\right]^2} = |\ell_2 - \ell_1| \sqrt{p\bar{\eta}(t)(1-\bar{\eta}(t))} \qquad [S12]$$

Note that, as σ_{ℓ_q} depends weakly on the harmonic order—the parameter p remains almost constant along the non-perturbative spectral plateau—, which infers that $\bar{\ell}_q(t)$ presents well-defined intermediate OAM states. Put another way, as the self-torqued harmonic beam is synthesized, the radiative recombinations leading to bright HHG emission progress through a ladder of photonic OAM states ($\bar{\ell}_q(t)$), which themselves are physical and quantized with a low relative error. We stress that this feature results from the non-perturbative behavior of HHG (p<q). On the other hand, in the case of perturbative nonlinear optics, the OAM width would be much larger than for HHG (Eq. S12, with p=q). This, together with the substantially lower values of q and ℓ_q associated with perturbative processes, would yield not only a lower—but also an ill-defined—self-torque.

The inset of Fig. 1 in the main text already shows the excellent agreement between Eqs. S11 and S12 and the full quantum simulations. In order to show how the self-torque is imprinted for different time delays, we present in Fig. S1 the results of our full quantum simulations for the time-dependent OAM evolution of the 17th harmonic when the time delay between the driving vortex fields ($\ell_1 = 1$ and $\ell_2 = 2$) is (A) $t_d = \frac{2}{3}\tau$ =6.66 fs, (B) $t_d = \frac{5}{6}\tau$ =8.33 fs, (C) $t_d = \tau$ =10 fs, and (D) $t_d = \frac{7}{6}\tau$ =11.66 fs, where $\tau = 10$ fs is the pulse duration at full width at half maximum (FHWM) and the rest of parameters are the same as in Fig. 1 of the main text. As indicated by the green lines, the mean OAM, $\bar{\ell}_{17}$ (solid lines) and the OAM width, $\sigma_{\ell_{17}}$ (dashed lines) faithfully follow the prediction given by Eqs. S11 and S12 at each temporal delay.

Two main observations can be obtained when looking at self-torqued beams generated using different time delays. First, the self-torque, ξ_{17}, increases with the time delay. This is confirmed by our experiments (see Fig. 3 of the main text). Second, we note that although in all cases self-torqued beams are generated, when the time delay is closer to the pulse duration ($t_d = \tau$, Fig. S1C), the OAM trace is more smooth and extends through a wider range of topological charges exhibiting similar weight, i.e., a time delay similar to the pulse duration is the optimal to generate self-torqued beams.

S2. Distinction Between Self-Torqued Beams and Time-Delayed Vortex Beams

In this section, we further stresses the difference between a self-torqued pulse, with OAM ranging from $q\ell_1$ and $q\ell_2$, and a pulse resulting from the mere superposition of two delayed vortex pulses, the first carrying $q\ell_1$ units of OAM and the second $q\ell_2$. While in both cases the mean OAM varies in time from $q\ell_1$ to $q\ell_2$, only the self-torqued beams include all the intermediate OAM contributions, thus containing *physical* photons of all the intermediate OAM states.

This distinction—which is evident in the OAM spectrum—also has unequivocal signatures in the temporal evolution of the phase and intensity profiles of the beams. In order to explore this aspect, we have performed high-spatial-resolution simulations of the HHG process. For this, the computational load is drastically reduced if a diffraction model is employed, instead of the exact full quantum simulation. The so-called Thin Slab

Model (TSM) considers the HHG medium as a thin (2D) slab perpendicular to the driving laser propagation. The harmonics are calculated using the analytic SFA representation introduced in Section S1 and propagated using Fraunhofer diffraction. The model has been proved to successfully reproduce detailed features of HHG driven by vortex beams (*16, 18, 20, 26*).

In Movie 1 of the main text, we presented the temporal evolution of the spatial phase, intensity, and OAM profiles for the two cases under study: the self-torqued 11th harmonic calculated through the TSM, and the mere superposition of two vortex beams carrying $\ell_i = q\ell_1 = 11$ and $\ell_f = q\ell_2 = 22$, delayed by $t_d = \tau = 10$ fs. Three instants of time for each case are captured in Figs. S3 and S4, respectively.

On one hand, the spatial phase distribution of the self-torqued harmonic beam—from which one can extract the OAM content by counting the number of phase branches—shows the continuous appearance of new vortex singularities along a single row, breaking the q-fold symmetry (which resembles to the phase structure reported when considering the appearance of new vortices as a Hilbert's Hotel paradox (*73*)). This reflects the continuous variation of OAM from $q\ell_1$=11 to $q\ell_2 = 22$. In addition, phase singularities are born one at a time (see Fig. S3D), conforming a topological structure where new vortices subsequently emerge. The intensity distribution follows the structure of the combination of vortex beams with subsequent OAM charges, $\ell_i + \ell_{i+1}$, canceling out in the spatial region where the phase singularities are placed (see Fig. S3E), and, thus, presenting a crescent shape, which evidences the presence of self-torqued beams.

On the other hand, the temporal evolution of the spatial phase and intensity distributions of the two time-delayed vortex beams remains q-fold symmetric, as the OAM content is the superposition of two components $q\ell_1$ and $q\ell_2$, with time-dependent weights. This symmetry is reflected in the spatial phase distribution, where all the new singularities appear simultaneously (see Fig. S4D). Moreover, the spatial intensity profile exhibits two clear radial rings, instead of the crescent shape (see Fig. S4E). The intensity profile evolves gradually from the ring shape of the vortex beam with $q\ell_1$ to that with $q\ell_2$, evidencing the absence of intermediate OAM contributions.

Our results show that there is a fundamental distinction between a field carrying ℓ OAM units—as one of the intermediate states in a self-torqued beam—, and the superposition of two modes of different topological charges, but same averaged-OAM, $\overline{\ell} = \ell$. These two kinds of beams have different essential physical properties, not only the OAM content but also the temporal evolution of the spatial phase and intensity. In particular, the crescent-shaped intensity distribution measured in our experiments (Fig. 3 and Figs. S7-8) is a clear signature of the generation of beams with self-torque.

S3. Additional Experimental Details for the Generation and Characterization of Self-Torqued EUV Beams

Self-torqued light beams are generated by driving HHG with an IR vortex driving beam comprised of a time-delayed superposition of two pure OAM modes (i.e., ℓ is an integer). Essential to both the generation and subsequent detection of the self-torque of light is the use of highly pure ultrafast vortex pulses, as well as a robust and stable beamline capable of maintaining subfemtosecond timing resolution and repeatability. Moreover, we require few-micron pointing stability over a relatively large range in delay times (~100 fs, for the 52 fs pulses used in this work). These demanding criteria are

realized by using a setup that employs a high-accuracy and high-precision delay stage (Newport XPS-160S), a modified, iterative phase-retrieval algorithm to optimize and quantify the modal purity of the dual-vortex driving beam (*74, 75*), and a home-built beam pointing stabilization system (*76*), which are described in more detail below.

In order to ensure precise overlap of the single-mode OAM driving beams, and thus the synthesis of a high-quality dual-OAM driver—also known in the literature as a "fractional" OAM beam—, independent circular apertures and lenses are placed in each arm of the Mach-Zehnder interferometer, which yield highly pure, single-mode OAM drivers with a similar intensity and waist size at focus. The quality of the driving beams, as well as their modal purity, are quantified by directing a small portion of the IR vortex beams onto a visible charge-coupled device (CCD) camera (Mightex BTE-B050-U) and recording intensity profiles as a function of propagation distance. These intensity profiles are then fed into a modified Gerchberg-Saxton (GS) phase-retrieval algorithm (*74, 75*), which reconstructs the complex, spatial amplitude of the beams with a high resolution (see Section S4 below).

A separate pair of visible CCD cameras is used to monitor fluctuations in beam pointing over the delay range of the experiment, and these fluctuations are minimized using a home-built beam pointing stabilization system (*76*). Briefly, the beam pointing stabilization system is comprised of two piezo-actuated mirror mounts (one in the amplifier itself, one at the entrance of the interferometer, ~4 m away), two additional CCD cameras, and a desktop computer that closes the digital feedback loop. The leak-through of the full, amplified beam upon hitting the last mirror before the interferometer is passed through a lens, and one camera monitors the beam centroid at focus while the other measures the far-field intensity centroid of the beam. The use of two independent feedback loops allows for control of not only the transverse position of the common focus of the OAM beams, but also the propagation angle, which ensures good overlap and collinearity between the two beams. Drifts in beam pointing on the two cameras are then compensated via an active, digital feedback loop that adjusts the tip and tilt of the piezo-actuated mirrors at a rate of ~100 Hz, ensuring that the OAM driving beams remain spatially overlapped throughout the duration of the experiment. Such a scheme yields few-micron repeatability and stability of the driving beams, with only small fluctuations occurring due to mechanical noise (e.g., thermal expansion of optomechanics, high-frequency vibrations, etc.) in the beamline.

S4. Characterization of IR Vortex Driving Modes via a Modified Gerchberg-Saxton Phase-Retrieval Algorithm

Essential to both the generation and subsequent detection (see below) of the self-torque of light is the use of highly pure, ultrafast driving vortex pulses. To assess the quality of these beams, as well as their combination, a wedge is translated into and out of the collinear focusing beams just after the exit of the interferometer, and the beam(s) are imaged onto a CCD camera (Mightex, BTE-B050-U). Beam profile images are recorded as a function of propagation distance, z, and then fed into a modified GS phase retrieval algorithm that is based on previous work in the literature (74, 75).

In our implementation of the GS algorithm, we first record a series of intensity images as a function of propagation distance, sampling from the focal point to at least two Rayleigh lengths on both sides of the focus. Since only the intensity is captured by a

camera, we use a phase-retrieval algorithm to extract the phase of the beam. The phase retrieval itself is over-constrained, meaning there is an optimal solution as well as additional degrees of freedom that can be used to evaluate and confirm the retrieval. In the first iteration, a uniform (i.e., flat) phase is applied to the square root of the recorded intensity in the first image, which serves as the initial guess for the complex electric field. This initial guess is numerically propagated to the plane of the next recorded image. At this plane, the amplitude of the retrieved beam is replaced by the observed amplitude, while preserving the retrieved phase. The algorithm continues to propagate to each plane where an image was taken, replacing the retrieved amplitude with the observed amplitude at each plane. Once the algorithm has incorporated all the images once, the final retrieved electric field is used as the initial guess for the next iteration. This entire process is repeated for up to 1,000 iterations, until the error between the retrieved and measured amplitudes reaches a global minimum. In order to ensure that the algorithm finds the correct OAM content without stalling in a local minimum, we apply an azimuthal phase perturbation of $\ell = \pm 1/2$ every 10 iterations (alternating the sign for each perturbation), for the first 100 iterations. These perturbations do not affect the retrieval of a Gaussian beam ($\ell = 0$), but greatly reduce the number of iterations needed to converge the retrieval for OAM beams. This algorithm correctly retrieved the phase of simulated data of a variety of superpositions of $\ell = \{0, 1, 2\}$ and the radial index $p = \{0, 1\}$ with and without random noise applied. Using this approach, we can reconstruct the complete complex amplitude of the vortex beams as a function of propagation distance (see Supplemental Movie S1) in under 5 minutes on a personal laptop computer (MacBook Pro, 16 GB RAM), with a resolution limited only by the CCD pixel size (in this case, 2.2 μm).

The intensity recorded by the CCD camera as a function of propagation distance, z, near the focus of each driving beam corresponds to the squared amplitude of a Laguerre-Gaussian (LG) laser beam with wavelength λ_0, ($k_0 = 2\pi/\lambda_0$),

$$LG_{\ell,p}(\rho, \phi, z; k_0) = E_0 \frac{w_0}{w(z)} \left(\frac{\sqrt{2}\rho}{w(z)}\right)^{|\ell|} L_p^{|\ell|}\left(\frac{2\rho^2}{w^2(z)}\right) \times \exp\left[-\frac{\rho^2}{w^2(z)}\right] \exp\left[i\ell\phi + i\frac{k_0\rho^2}{2R(z)} + i\Phi_G(z)\right] \quad \text{[S13].}$$

Here, $w(z) = w_0\sqrt{1 + (z/z_0)^2}$ is the beam waist, with w_0 being the beam waist at focus and $z_0 = \pi w_0^2/\lambda_0$ the Rayleigh range with wavelength λ_0, ($k_0 = 2\pi/\lambda_0$), $R(z) = z[1 + (z_0/z)^2]$ is the phase-front radius, $\Phi_G(z) = -(2p + |\ell| + 1)\arctan(z/z_0)$ is the Gouy phase, and $L_p^{|\ell|}(x)$ are the associated Laguerre polynomials (3). The indices $\ell = 0, \pm 1, \pm 2, \ldots$ and $p = 0, 1, 2, \ldots$ correspond to the topological charge and the number of nonaxial radial nodes of the mode, respectively. In experiments, Eq. S13 does not strictly apply and real LG beams are described by a summation of LG modes with a common waist size, but varying mode indices. As such, the purity of an OAM beam is quantified by the power of the desired topological charge divided the power of the entire OAM spectrum of the beam (note that the same is true of any beam possessing azimuthally varying phase, e.g., hypergeometric gaussian beams (77)). In order to obtain the OAM spectrum, we perform a Fourier transform over the azimuthal coordinate of the reconstructed complex amplitude of the driving beams (Fig. S5A-C), which is more general and efficient than modal decomposition algorithms (20, 78). The resulting OAM

spectra show that highly pure vortex driving modes with little radial mode character are obtained for the ℓ_1 and ℓ_2 drivers, leading to a high quality, dual-OAM vortex beam for driving the HHG process (Fig. S5D-F). Overall, we find that 95% (93%) of the total power in the ℓ_1 (ℓ_2) driver is contained within the ℓ = 1 (2) mode (Fig. S5G-I). We note that the GS algorithm is ambiguous with respect to the absolute sign of ℓ; however, the relative sign between the two beams non-ambiguous. For this work, ℓ_1 and ℓ_2 have the same sign, which is confirmed to be positive via an independent measurement of the OAM sign by using a cylindrical lens as 1D Fourier transform element (79). Finally, the reconstructed beams can be propagated arbitrarily in space, which allows us to inspect the beam quality both before and after the focus (see Supplemental Movie S1).

S5. Control of IR and HHG Beam Pointing with a Time-Delayed Combination of Vortex Driving Beams

The quantitative measurement of the self-torque of the experimentally generated EUV beams requires a high precision measurement of either the induced azimuthal frequency chirp, or the ultrafast variation of OAM on the subfemtosecond time scale. Since the latter is currently unfeasible with existing technologies, the azimuthal frequency chirp is instead measured by exploiting both the physics of time-dependent OAM and the optics of the EUV spectrometer system (see Fig. 3 in the main text). However, such a scheme demands few-micron spatial control of the HHG beam pointing, which we achieve by exploiting the optics of multicomponent OAM beams.

Vortex beams comprised of the superposition of two (or more) LG beams with differing topological charges, but same size of the intensity ring, exhibit exotic amplitude and phase distributions that can be controlled by either the phase delay between the constituent waveforms, or the topological charge in each beam (3). In the experiment, the HHG driving vortex beam is synthesized from two ultrafast pulses with topological charges of $\ell_1 = 1$ and $\ell_2 = 2$—as well as equal in amplitude and spatial extent—, which results in a non-pure vortex beam with a characteristic "crescent" shape to the intensity distribution (see Fig. S5A-C, Fig. S6, and Fig. 2 and 3 of the main text). The angular direction of the center-of-mass (COM) of the intensity crescent can be controlled via a relative phase delay between the two single-mode OAM drivers, such that a full-cycle phase delay (e.g., 2.635 fs for the 790 nm pulses used here) returns the intensity crescent to its initial position. By carefully adjusting the time delay between the two single-mode IR vortex beams, we can control the alignment of the driving intensity crescent with few-micron precision (Fig. S6B, limited by the 2.2 μm pixel size of the visible CCD camera). Since, to first order, the HHG beam profile mimics the intensity distribution of the driving beams, we can simultaneously and precisely align the HHG intensity crescent (Fig. S6C) to the dispersion axis of the spectrometer, which naturally maps the azimuthal frequency variation to the spectral dimension of the dispersed HHG spectra (see Fig. 3 of the main text). This naturally yields a high-resolution measurement of both the azimuthal extent of the beam, as well as the self-torque-induced azimuthal frequency variation, without the need for measuring the subfemtosecond variation of the azimuthal phase in the EUV.

S6. Extraction of the Azimuthal Angle Subtended by the EUV HHG Beams

In order to compute the self-torque of the experimentally generated EUV beams, both the spectral shift and azimuthal angle subtended by the harmonics needs to be measured with high precision. To extract the azimuthal angle of the HHG beam, we measure the raw HHG beam profile at the flat-field-image plane of the spectrometer with a high-pixel-density EUV CCD camera (Andor, Newton 940, 512x2, 048 pixels, 13.5 μm pitch). The HHG intensity crescent subtends a small arc of a uniform circle—the center of which occurs at the common singularity of the OAM harmonics generated by the individual $\ell_1$and ℓ_2 drivers (represented by a white dot in Fig. S7)—and we use the properties of a uniform circle to extract the azimuthal angle.

For a uniform circle of radius, r, the chord length, a, between the two extrema of a circular section (i.e., arc) is given by $a = 2r\sin(\phi/2)$, where ϕ is the central angle of the arc and, in this case, the azimuthal angle subtended by the HHG beam (Fig. S7A). By measuring the radius of the inscribed circle and the length of the chord between the e^{-4} intensity points of the beam, we can extract both the chord length and radius of the high-order harmonic beam. Then, using the known relation for the chord length as a function of radius and central (azimuthal) angle, we can extract the full azimuthal angular range of the high-order harmonics, with a high precision (Fig. S7B).

S7. Verification of Experimental Scheme to Measure the Azimuthal Frequency Chirp of Self-Torqued EUV Beams

Measurement of the self-torque of EUV beams relies on extracting both the azimuthal angle subtended by the HHG beam and the spectral shift of each harmonic in the HHG spectrum, at each time delay. In order to validate that the spectral shift arises from the self-torque and not an artifact of the imaging conditions of EUV spectrometer or dynamics of the HHG up-conversion process, we present in Fig. S8A and S8B the HHG spectra obtained at a delay where the self-torque is maximized, and at near-zero delay, respectively. Clearly, the azimuthal frequency shift is only observed when the pulses are delayed by a sufficient amount. As a further verification of the self-torque-induced azimuthal frequency chirp, we also drove HHG with the single-mode OAM beams comprising the dual-OAM driving vortex beam. Taken together, the dispersed harmonic spectra (Fig. S8A-D) show that the azimuthal spectral shift of the high-order harmonics is only found when driving the up-conversion process with a time-delayed, dual-vortex mode. Moreover, the single mode spectra (Figs. S8C-D and Figs. S8G-H) show that the observed spectral shifts are not the result of over-driving the HHG process, as similar cutoffs and azimuthal ranges are obtained for the self-torqued HHG beams (Figs. S8A-B).

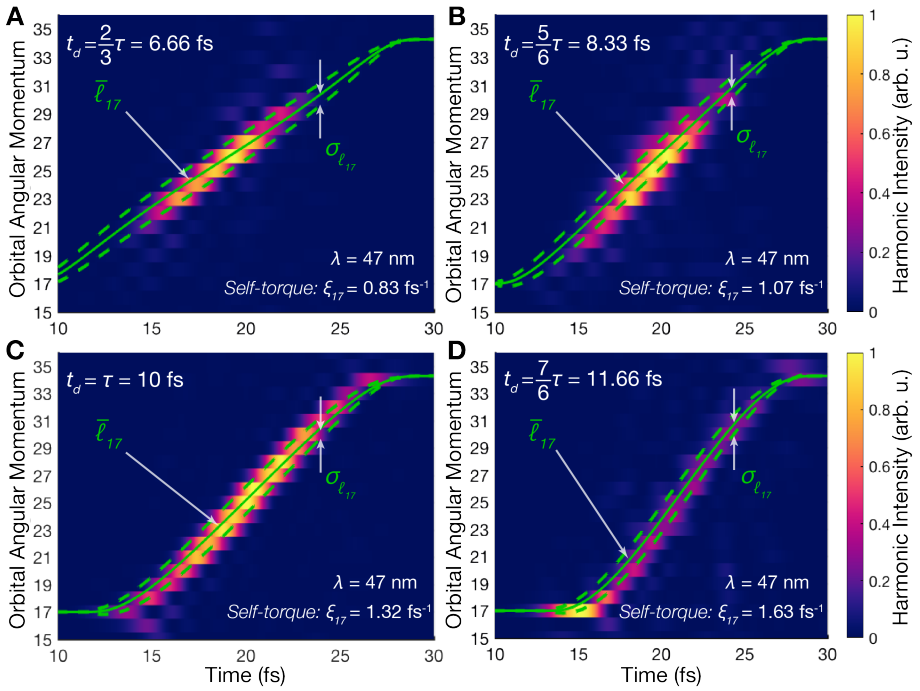

Fig. S1. Temporal Evolution of the OAM for Different Time Delays.

Computed OAM of the 17th harmonic beam generated by two 800 nm driving pulses (ℓ_1= 1 and ℓ_2= 2) with duration, τ = 10 fs, for different time delays: (**A**) $t_d = \frac{2}{3}\tau$ = 6.66 fs, (**B**) $t_d = \frac{5}{6}\tau$ = 8.33 fs, (**C**) $t_d = \tau$ = 10 fs, (**D**) $t_d = \frac{7}{6}\tau$ = 11.66 fs. The color background shows the results from the full quantum simulations, whereas the mean OAM, $\bar{\ell}_{17}$ (solid green), and the width of the OAM distribution, σ_{17} (dashed-green line), are obtained from Eqs. S11 and S12. The self-torque, ξ_{17}, is obtained from the slope of the time-dependent OAM.

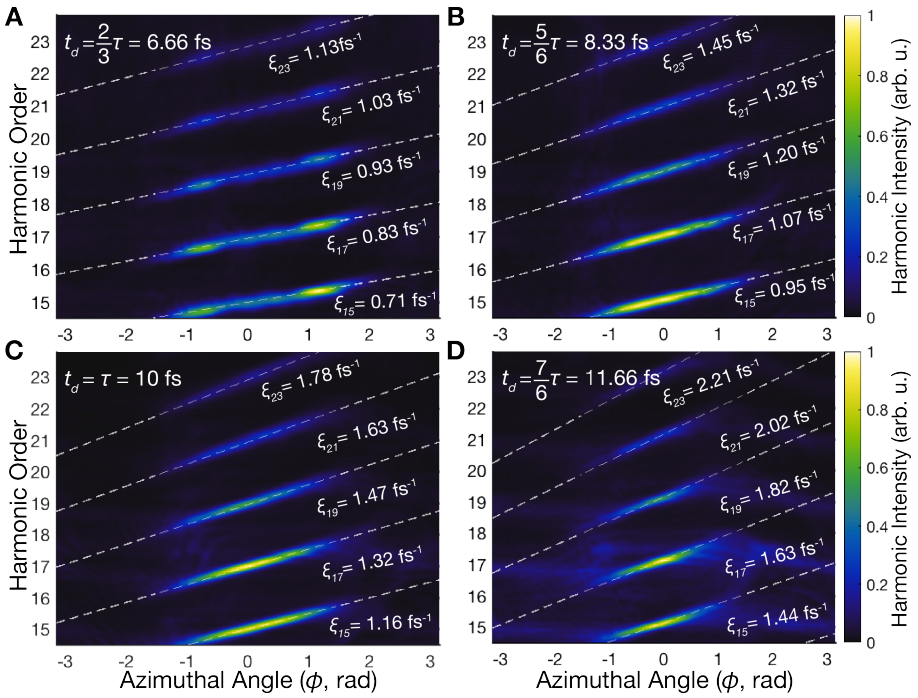

Fig. S2. Azimuthal Chirp of Self-Torqued Beams for Different Time Delays.

Spatial HHG spectrum along the azimuthal coordinate (ϕ) obtained from our full quantum simulations. The driving pulses, centered at 800 nm, with ℓ_1= 1 and ℓ_2= 2 and pulse duration, $\tau = 10$ fs, for different time delays: (**A**) $t_d = \frac{2}{3}\tau$ = 6.66 fs, (**B**) $t_d = \frac{5}{6}\tau$ = 8.33 fs, (**C**) $t_d = \tau$ = 10 fs, (**D**) $t_d = \frac{7}{6}\tau$ = 11.66 fs. The light self-torque imprints an azimuthal frequency chirp, which is different for each harmonic order, and each time delay, as indicated by the grey dashed lines (obtained from Eq. 6 in the main text).

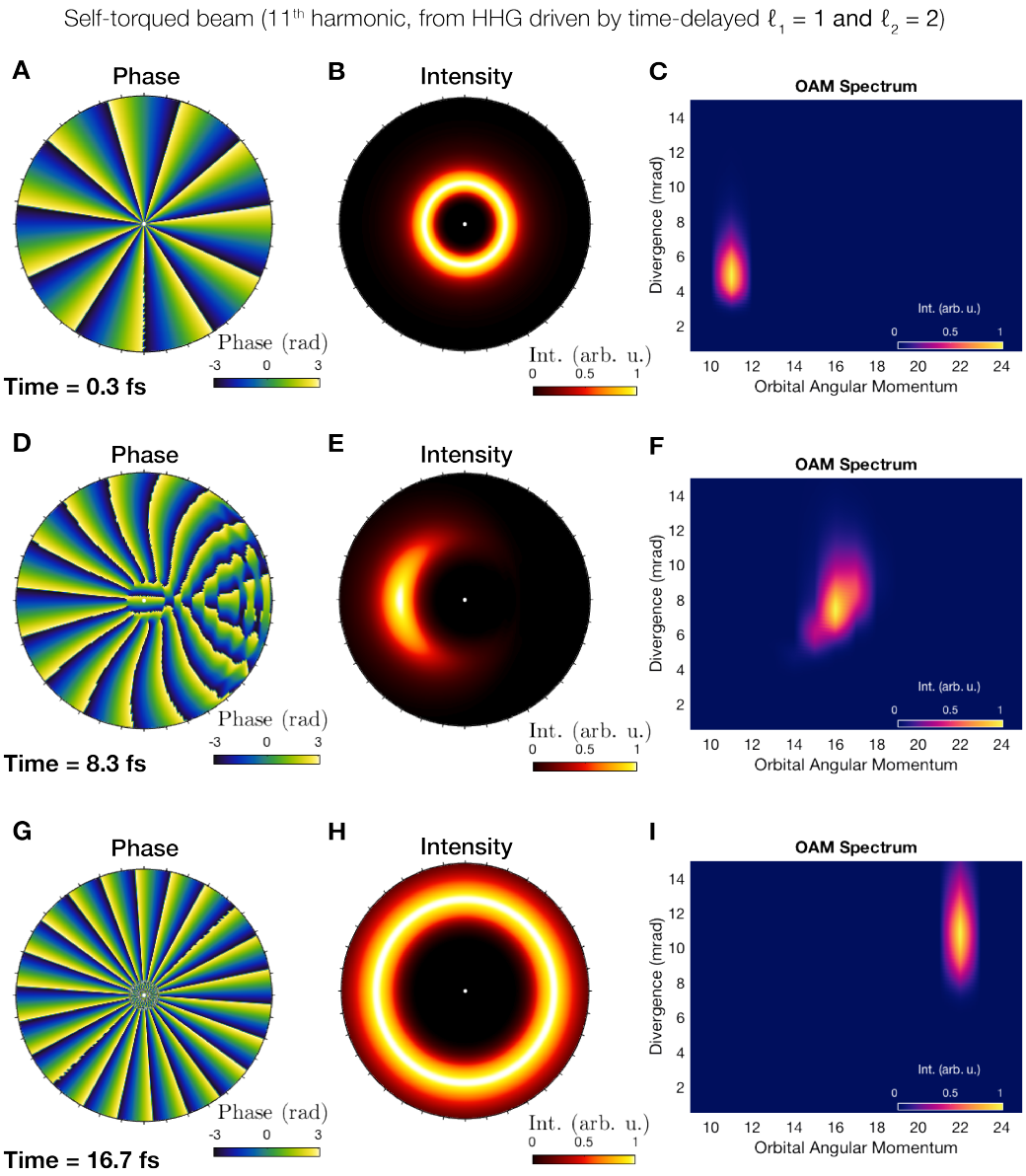

Fig. S3. Temporal Evolution of Phase, Intensity and OAM Content of Self-Torqued Beams.

Phase (**A**, **D**, **G**) intensity (**B**, **E**, **H**) and OAM distribution along the divergence (**C**, **F**, **I**) at three different instants of time: the initial state (**A-C**, t=0.3 fs), an intermediate state (**D-F**, t=8.3 fs) and the final state (**G-I**, t=16.7 fs) for a self-torqued beam generated through HHG ($\ell_1 = 1, \ell_2 = 2, \tau = 10$ fs, $t_d = 10$ fs, $\lambda_1 = \lambda_2 = 800$ nm). These results have been calculated using the TSM and the panels are snapshots from the Movie 1.

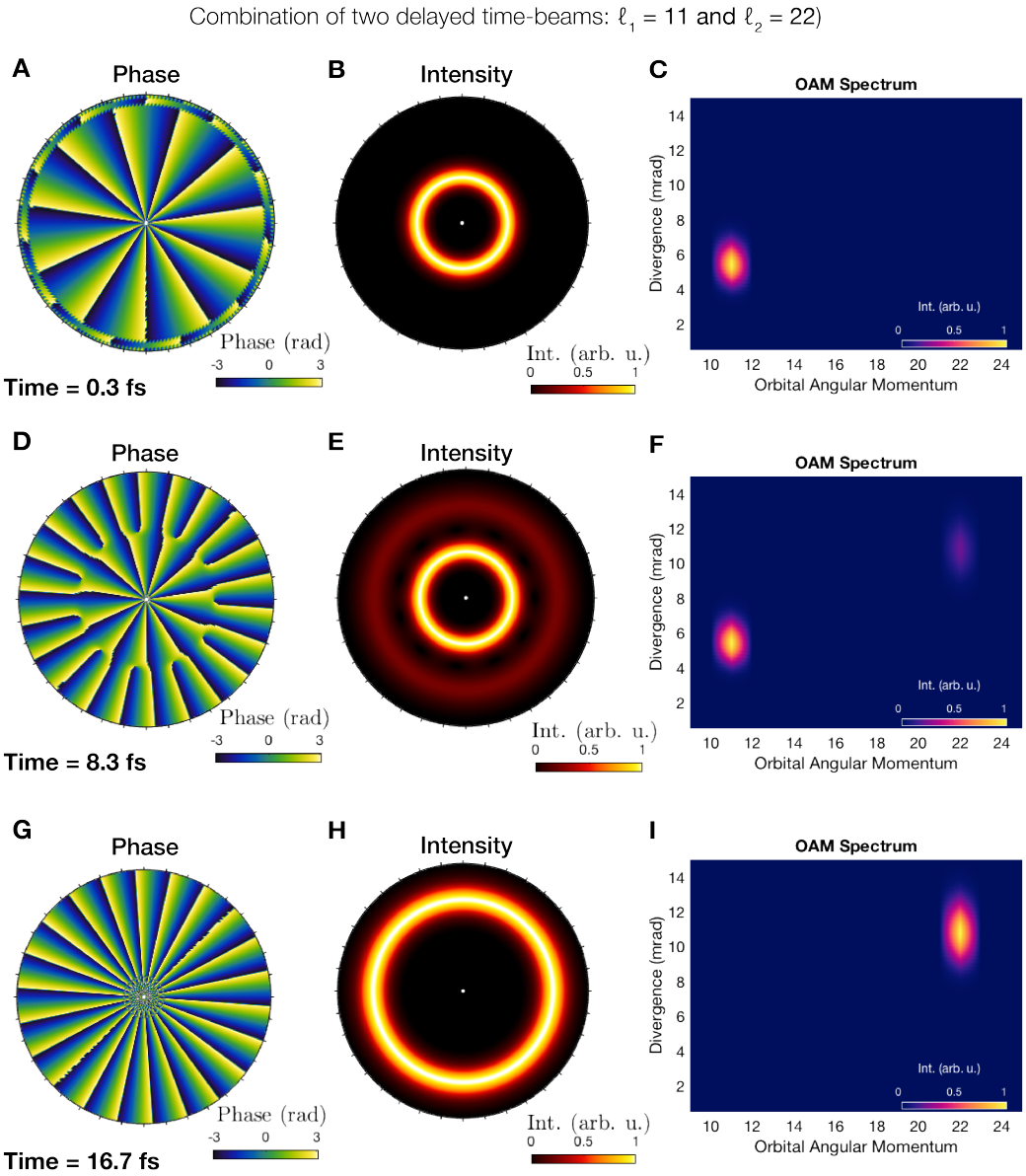

Fig. S4. Temporal Evolution of Phase, Intensity and OAM Content of Two Delayed Vortex Beams.

Phase (**A**, **D**, **G**) intensity (**B**, **E**, **H**) and OAM distribution along the divergence (**C**, **F**, **I**) at different instants of time: the initial state (**A-C**, t=0.3 fs), an intermediate state (**D-F**, t=8.3 fs) and the final state (**G-I**, t=16.7 fs) for the combination of two delayed vortex beams ($\ell_1 = 11$, $\ell_2 = 22$, $\tau = 10$ fs, $t_d = 10$ fs, $\lambda_1 = \lambda_2 = 800$ nm). The panels are snapshots from the Movie 1.

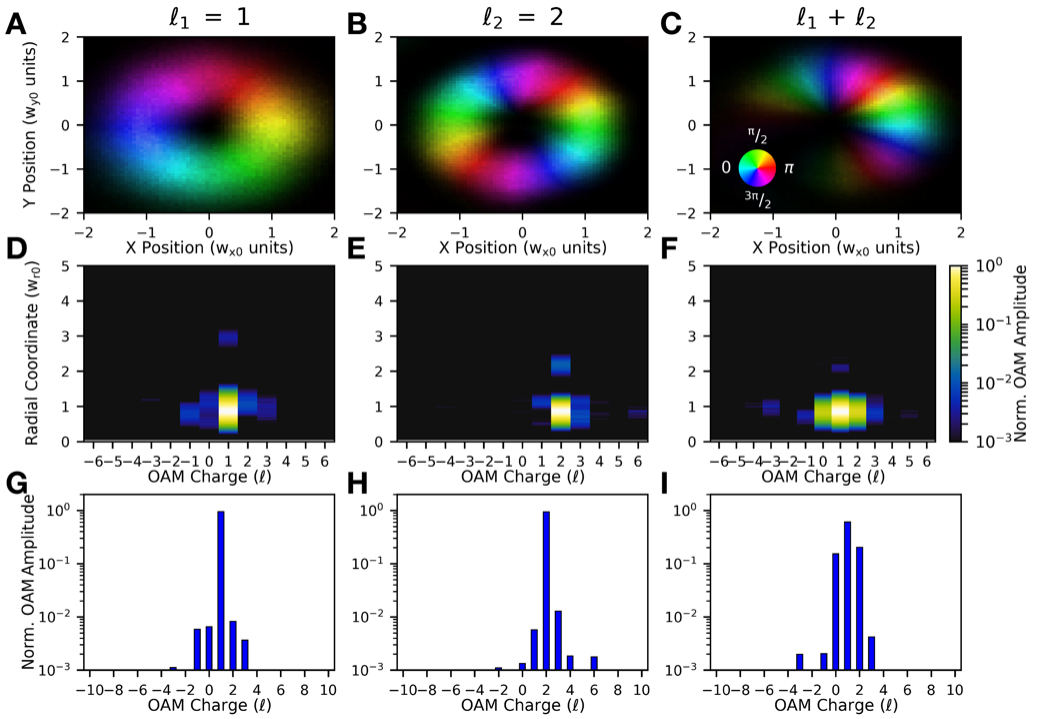

Fig. S5. Experimental Characterization of Pure and Non-Pure IR Vortex Beams.

The GS algorithm reconstructs the complex amplitudes of the ℓ_1 and ℓ_2 driving beams, and the combined HHG driver, with a high resolution and accuracy. (**A-C**), The reconstructed wavefronts of the IR vortex beams show that each constituent waveform is comprised of an integer number of phase wraps across a uniform intensity ring, while the OAM-combined HHG driver manifests as an intensity "crescent" with a non-integer number of phase wraps. In (**A-C**), amplitude is represented as saturation and value (i.e., brightness), and phase is represented by color (i.e., hue), with the corresponding phase values indicated by the color wheel in (**C**). (**D-F**), The radial OAM spectrum obtained via an azimuthal Fourier transform of the complex amplitudes in (**A-C**) show that all beams possess little radial mode character, with nearly all of the OAM content being contained within the primary intensity ring. (**G-I**), The radially integrated OAM spectra confirm the high purity of the experimental OAM beams, showing a modal purity of 95% and 93% for the ℓ_1 and ℓ_2 drivers, respectively.

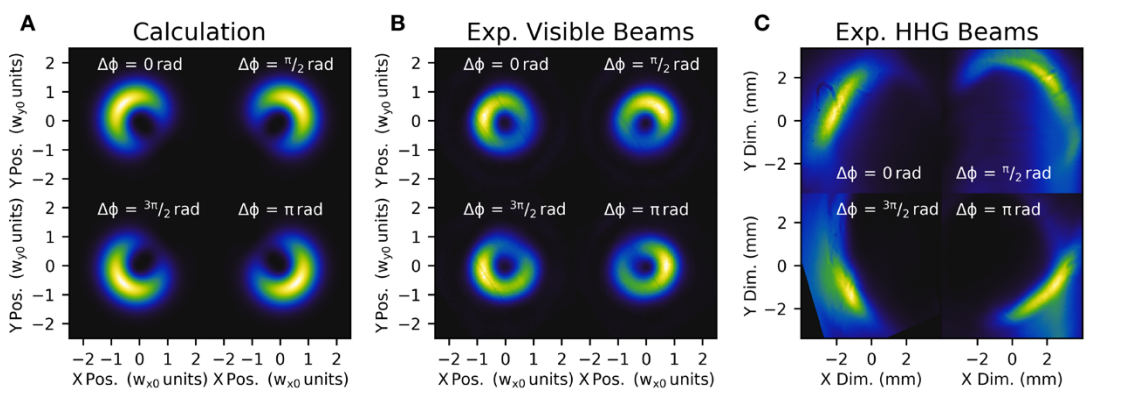

Fig. S6. Control of IR and HHG Beam Alignment via the Relative Phase Delay of the Single-Mode OAM Driving Beams.

(**A**), When single-mode OAM beams with topological charges of $\ell_1 = 1$ and $\ell_2 = 2$ are superposed with the same amplitude and waist size, a crescent-shaped intensity distribution is obtained with a directionality determined by the relative phase delay between the two beams. (**B**), In the experiment, the relative time delay between the two beams is used to control the phase delay (and thus, the COM position of the visible beam) with attosecond and few-micron precision. (**C**), The control over the visible beams translates directly to the HHG beams, allowing for precise alignment of the HHG crescent to the dispersion axis of the spectrometer. In the lower left of panel c, the HHG beam is partially clipped by the filter housing before the EUV CCD camera.

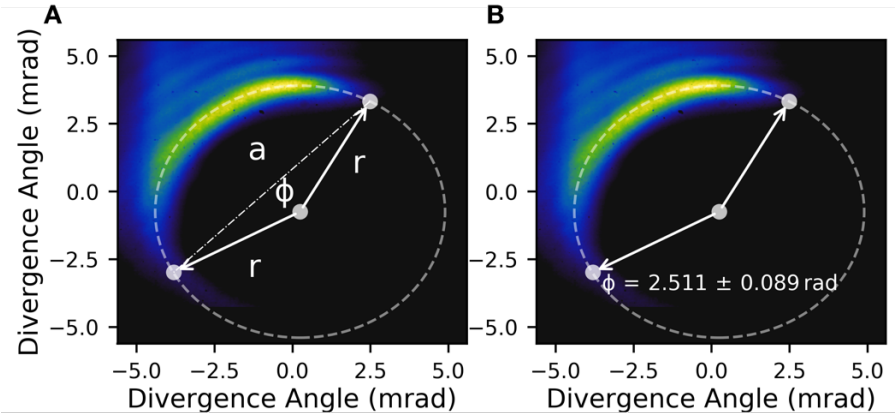

Fig. S7. Extraction of the Azimuthal Angular Range of Self-Torque EUV High-Order Harmonics.

The intensity crescent formed by the self-torqued EUV high-harmonics can be inscribed by a uniform circle of radius, *r*. (**A**), The HHG beam profile subtends a circular section (i.e., arc) of this uniform circle defined by a central (i.e., azimuthal) angle, ϕ, and the e^{-4} intensity points of this arc define a chord length, *a*. (**B**), Using the equations relating *r, a,* and ϕ for a uniform circle, we can extract the azimuthal angle of the HHG beam with a high precision. Note that the center of this circle occurs at the common singularity of the OAM harmonics generated from the individual drivers (represented by a white dot in both panels).

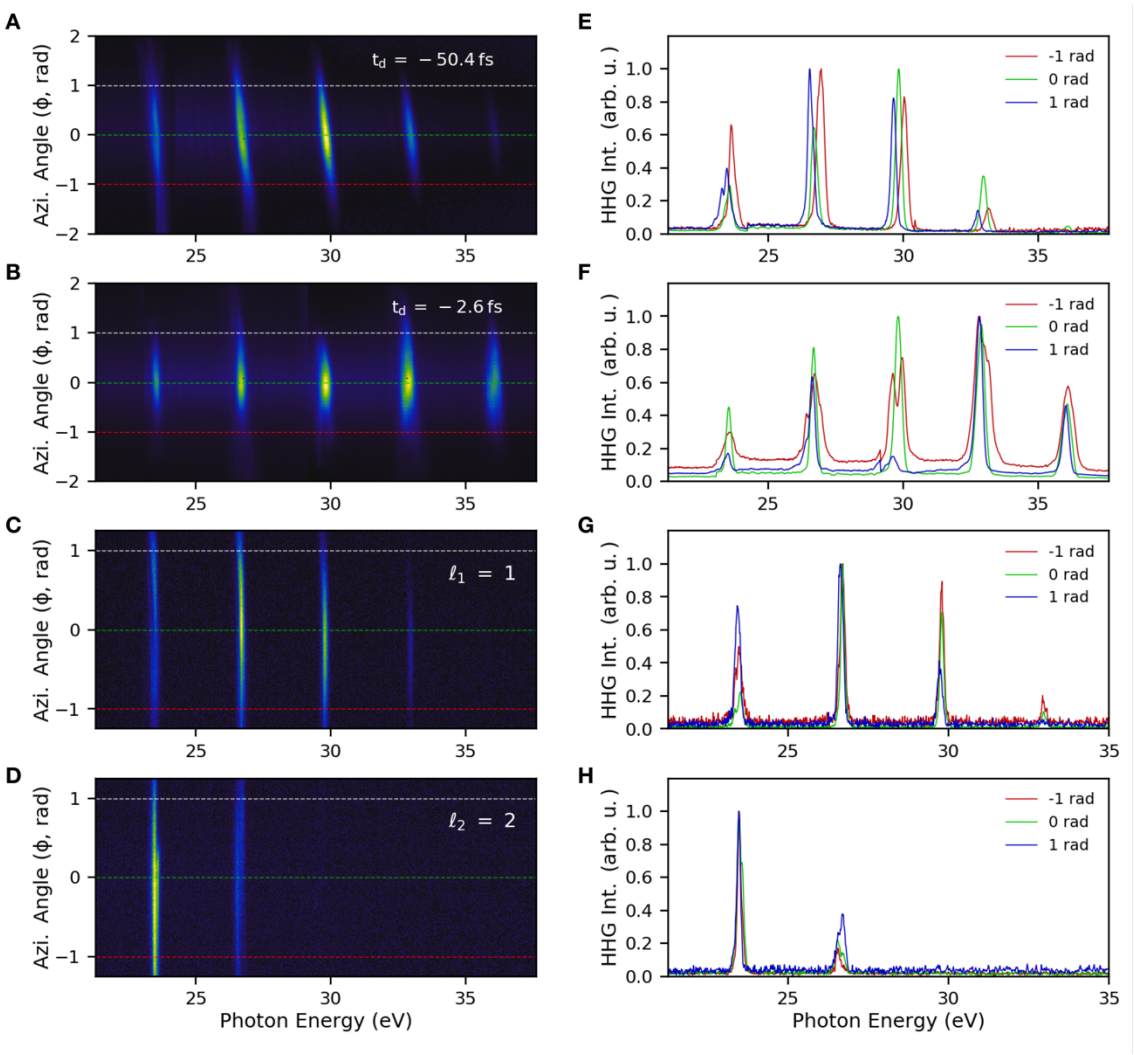

Fig. S8. Experimental Confirmation of the Spectral Shift Induced by the Self-Torque of Light.

An EUV CCD camera records the dispersed OAM HHG spectrum at the flat-field imaging plane of the EUV spectrometer, yielding a spatiospectral image of the emitted harmonics. (**A**-**D**), The HHG spectra for the combined beam at (**A**) -50.4 fs and, (**B**) -2.6 fs, delay and the individual OAM drivers (**C**-**D**) clearly show that the azimuthal frequency chirp is only present when HHG is driven with a non-pure vortex mode composed of two pulses separated by a time delay comparable to their pulse widths. (**E**-**H**), Azimuthally integrated HHG spectra at different azimuthal angles across the EUV spatial-spectrograms (shown in (**A**-**D**)) confirms the spectral shift observed in **A**, while the similar linewidths and cutoffs indicate that the spectral shift does not originate from overdriving the HHG process (e.g., ionization saturation, spatiotemporal reshaping of the driving beam, etc.).

Movie S1. Amplitude, Phase, and Intensity Evolution of the Reconstructed, Complex Beam Amplitudes for the Individual OAM Beams and Their Superposition

Reconstructed amplitude (top row), phase (middle row), and intensity (bottom row) of the individual (ℓ_1; left-column, ℓ_2; middle-column) and combined ($\ell_1 + \ell_2$; right-column) IR, LG driving beams, numerically propagated over the full Rayleigh range of each beam. The reconstructed beams exhibit a high degree of LG modal purity, which confirms the high-quality of the beams for driving the HHG process.

References and Notes

1. H. Rubinsztein-Dunlop, A. Forbes, M. V. Berry, M. R. Dennis, D. L. Andrews, M. Mansuripur, C. Denz, C. Alpmann, P. Banzer, T. Bauer, E. Karimi, L. Marrucci, M. Padgett, M. Ritsch-Marte, N. M. Litchinitser, N. P. Bigelow, C. Rosales-Guzmán, A. Belmonte, J. P. Torres, T. W. Neely, M. Baker, R. Gordon, A. B. Stilgoe, J. Romero, A. G. White, R. Fickler, A. E. Willner, G. Xie, B. McMorran, A. M. Weiner, Roadmap on structured light. *J. Opt.* **19**, 013001 (2017). doi:10.1088/2040-8978/19/1/013001

2. L. Allen, M. W. Beijersbergen, R. J. C. Spreeuw, J. P. Woerdman, Orbital angular momentum of light and the transformation of Laguerre-Gaussian laser modes. *Phys. Rev. A* **45**, 8185–8189 (1992). doi:10.1103/PhysRevA.45.8185 Medline

3. A. M. Yao, M. J. Padgett, Orbital angular momentum: Origins, behavior and applications. *Adv. Opt. Photonics* **3**, 161–204 (2011). doi:10.1364/AOP.3.000161

4. A. E. Willner, H. Huang, Y. Yan, Y. Ren, N. Ahmed, G. Xie, C. Bao, L. Li, Y. Cao, Z. Zhao, J. Wang, M. P. J. Lavery, M. Tur, S. Ramachandran, A. F. Molisch, N. Ashrafi, S. Ashrafi, Optical communication using orbital angular momentum beams. *Adv. Opt. Photonics* **7**, 66–106 (2015). doi:10.1364/AOP.7.000066

5. A. Trichili, C. Rosales-Guzmán, A. Dudley, B. Ndagano, A. Ben Salem, M. Zghal, A. Forbes, Optical communication beyond orbital angular momentum. *Sci. Rep.* **6**, 27674 (2016). doi:10.1038/srep27674 Medline

6. S. Fürhapter, A. Jesacher, S. Bernet, M. Ritsch-Marte, Spiral phase contrast imaging in microscopy. *Opt. Express* **13**, 689–694 (2005). doi:10.1364/OPEX.13.000689 Medline

7. M. A. Lauterbach, M. Guillon, A. Soltani, V. Emiliani, STED microscope with spiral phase contrast. *Sci. Rep.* **3**, 2050 (2013). doi:10.1038/srep02050 Medline

8. G. Vicidomini, P. Bianchini, A. Diaspro, STED super-resolved microscopy. *Nat. Methods* **15**, 173–182 (2018). doi:10.1038/nmeth.4593 Medline

9. M. Padgett, R. Bowman, Tweezers with a twist. *Nat. Photonics* **5**, 343–348 (2011). doi:10.1038/nphoton.2011.81

10. J. P. Torres, L. Torner, *Twisted Photons: Applications of Light with Orbital Angular Momentum.* (Bristol: Wiley-VCH, 2011).

11. L. Marrucci, C. Manzo, D. Paparo, Optical spin-to-orbital angular momentum conversion in inhomogeneous anisotropic media. *Phys. Rev. Lett.* **96**, 163905 (2006). doi:10.1103/PhysRevLett.96.163905 Medline

12. M. W. Beijersbergen, R. P. C. Coerwinkel, M. Kristensen, J. P. Woerdman, Helical-wavefront laser beams produced with a spiral phase plate. *Opt. Commun.* **112**, 321–327 (1994). doi:10.1016/0030-4018(94)90638-6

13. J. Atencia, M.-V. Collados, M. Quintanilla, J. Marín-Sáez, Í. J. Sola, Holographic optical element to generate achromatic vortices. *Opt. Express* **21**, 21056–21061 (2013). doi:10.1364/OE.21.021056 Medline

14. J. C. T. Lee, S. J. Alexander, S. D. Kevan, S. Roy, B. J. McMorran, Laguerre-Gauss and Hermite-Gauss soft x-ray states generated using diffractive optics. *Nat. Photonics* **13**, 205–209 (2019). doi:10.1038/s41566-018-0328-8

15. M. Zürch, C. Kern, P. Hansinger, A. Dreischuh, C. Spielmann, Strong-field physics with singular light beams. *Nat. Phys.* **8**, 743–746 (2012). doi:10.1038/nphys2397

16. C. Hernández-García, A. Picón, J. San Román, L. Plaja, Attosecond extreme ultraviolet vortices from high-order harmonic generation. *Phys. Rev. Lett.* **111**, 083602 (2013). doi:10.1103/PhysRevLett.111.083602 Medline

17. G. Gariepy, J. Leach, K. T. Kim, T. J. Hammond, E. Frumker, R. W. Boyd, P. B. Corkum, Creating high-harmonic beams with controlled orbital angular momentum. *Phys. Rev. Lett.* **113**, 153901 (2014). doi:10.1103/PhysRevLett.113.153901 Medline

18. C. Hernández-García, J. San Román, L. Plaja, A. Picón, Quantum-path signatures in attosecond helical beams driven by optical vortices. *New J. Phys.* **17**, 093029 (2015). doi:10.1088/1367-2630/17/9/093029

19. R. Géneaux, A. Camper, T. Auguste, O. Gobert, J. Caillat, R. Taïeb, T. Ruchon, Synthesis and characterization of attosecond light vortices in the extreme ultraviolet. *Nat. Commun.* **7**, 12583 (2016). doi:10.1038/ncomms12583 Medline

20. L. Rego, J. San Román, A. Picón, L. Plaja, C. Hernández-García, Nonperturbative twist in the generation of extreme-ultraviolet vortex beams. *Phys. Rev. Lett.* **117**, 163202 (2016). doi:10.1103/PhysRevLett.117.163202 Medline

21. A. Turpin, L. Rego, A. Picón, J. San Román, C. Hernández-García, Extreme ultraviolet fractional orbital angular momentum beams from high harmonic generation. *Sci. Rep.* **7**, 43888 (2017). doi:10.1038/srep43888 Medline

22. F. Kong, C. Zhang, F. Bouchard, Z. Li, G. G. Brown, D. H. Ko, T. J. Hammond, L. Arissian, R. W. Boyd, E. Karimi, P. B. Corkum, Controlling the orbital angular momentum of high harmonic vortices. *Nat. Commun.* **8**, 14970 (2017). doi:10.1038/ncomms14970 Medline

23. D. Gauthier, P. R. Ribič, G. Adhikary, A. Camper, C. Chappuis, R. Cucini, L. F. DiMauro, G. Dovillaire, F. Frassetto, R. Géneaux, P. Miotti, L. Poletto, B. Ressel, C. Spezzani, M.

Stupar, T. Ruchon, G. De Ninno, Tunable orbital angular momentum in high-harmonic generation. *Nat. Commun.* **8**, 14971 (2017). doi:10.1038/ncomms14971 Medline

24. C. Hernández-García, A twist in coherent X-rays. *Nat. Phys.* **13**, 327–329 (2017). doi:10.1038/nphys4088

25. R. Géneaux, C. Chappuis, T. Auguste, S. Beaulieu, T. T. Gorman, F. Lepetit, L. F. DiMauro, T. Ruchon, Radial index of Laguerre-Gaussian modes in high-order-harmonic generation. *Phys. Rev. A* **95**, 051801 (2017). doi:10.1103/PhysRevA.95.051801

26. K. M. Dorney, L. Rego, N. J. Brooks, J. San Román, C.-T. Liao, J. L. Ellis, D. Zusin, C. Gentry, Q. L. Nguyen, J. M. Shaw, A. Picón, L. Plaja, H. C. Kapteyn, M. M. Murnane, C. Hernández-García, Controlling the polarization and vortex charge of attosecond high-harmonic beams via simultaneous spin-orbit momentum conservation. *Nat. Photonics* **13**, 123–130 (2019). doi:10.1038/s41566-018-0304-3

27. W. Paufler, B. Böning, S. Fritzsche, Tailored orbital angular momentum in high-order harmonic generation with bicircular Laguerre-Gaussian beams. *Phys. Rev. A***98**, 011401 (2018). doi:10.1103/PhysRevA.98.011401

28. E. Pisanty, L. Rego, J. San Román, A. Picón, K. M. Dorney, H. C. Kapteyn, M. M. Murnane, L. Plaja, M. Lewenstein, C. Hernández-García, Conservation of torus-knot angular momentum in high-order harmonic generation. *Phys. Rev. Lett.* **122**, 203201 (2019). doi:10.1103/PhysRevLett.122.203201 Medline

29. M. Babiker, W. L. Power, L. Allen, Light-induced torque on moving atoms. *Phys. Rev. Lett.* **73**, 1239–1242 (1994). doi:10.1103/PhysRevLett.73.1239 Medline

30. H. He, M. E. Friese, N. R. Heckenberg, H. Rubinsztein-Dunlop, Direct observation of transfer of angular momentum to absorptive particles from a laser beam with a phase singularity. *Phys. Rev. Lett.* **75**, 826–829 (1995). doi:10.1103/PhysRevLett.75.826 Medline

31. A. T. O'Neil, M. J. Padgett, Three-dimensional optical confinement of micron-sized metal particles and the decoupling of the spin and orbital angular momentum within an optical spanner. *Opt. Commun.* **185**, 139–143 (2000). doi:10.1016/S0030-4018(00)00989-5

32. D. M. Villeneuve, S. A. Aseyev, P. Dietrich, M. Spanner, M. Yu. Ivanov, P. B. Corkum, Forced molecular rotation in an optical centrifuge. *Phys. Rev. Lett.* **85**, 542–545 (2000). doi:10.1103/PhysRevLett.85.542 Medline

33. D. G. Grier, A revolution in optical manipulation. *Nature* **424**, 810–816 (2003). Medline

34. M. E. J. Friese, H. Rubinsztein-Dunlop, J. Gold, P. Hagberg, D. Hanstorp, Optically driven micromachine elements. *Appl. Phys. Lett.* **78**, 547–549 (2001). doi:10.1063/1.1339995

35. E. M. Wright, J. Arlt, K. Dholakia, Toroidal optical dipole traps for atomic Bose-Einstein condensates using Laguerre-Gaussian beams. *Phys. Rev. A* **63**, 013608 (2000). doi:10.1103/PhysRevA.63.013608

36. A. Turpin, J. Polo, Y. V. Loiko, J. Küber, F. Schmaltz, T. K. Kalkandjiev, V. Ahufinger, G. Birkl, J. Mompart, Blue-detuned optical ring trap for Bose-Einstein condensates based on conical refraction. *Opt. Express* **23**, 1638–1650 (2015). doi:10.1364/OE.23.001638 Medline

37. A. F. Rañada, L. Vázquez, On the self-torque on an extended classical charged particle. *J. Phys. Math. Gen.* **17**, 2011–2016 (1984). doi:10.1088/0305-4470/17/10/013

38. S. R. Dolan, N. Warburton, A. I. Harte, A. Le Tiec, B. Wardell, L. Barack, Gravitational self-torque and spin precession in compact binaries. *Phys. Rev. D Part. Fields Gravit. Cosmol.* **89**, 064011 (2014). doi:10.1103/PhysRevD.89.064011

39. K. J. Schafer, B. Yang, L. F. DiMauro, K. C. Kulander, Above threshold ionization beyond the high harmonic cutoff. *Phys. Rev. Lett.* **70**, 1599–1602 (1993). doi:10.1103/PhysRevLett.70.1599 Medline

40. P. B. Corkum, Plasma perspective on strong field multiphoton ionization. *Phys. Rev. Lett.* **71**, 1994–1997 (1993). doi:10.1103/PhysRevLett.71.1994 Medline

41. A. Rundquist, C. G. Durfee 3rd, Z. Chang, C. Herne, S. Backus, M. M. Murnane, H. C. Kapteyn, Phase-matched generation of coherent soft x-rays. *Science* **280**, 1412–1415 (1998). doi:10.1126/science.280.5368.1412 Medline

42. R. A. Bartels, A. Paul, H. Green, H. C. Kapteyn, M. M. Murnane, S. Backus, I. P. Christov, Y. Liu, D. Attwood, C. Jacobsen, Generation of spatially coherent light at extreme ultraviolet wavelengths. *Science* **297**, 376–378 (2002). doi:10.1126/science.1071718 Medline

43. T. Popmintchev, M.-C. Chen, D. Popmintchev, P. Arpin, S. Brown, S. Alisauskas, G. Andriukaitis, T. Balciunas, O. D. Mücke, A. Pugzlys, A. Baltuska, B. Shim, S. E. Schrauth, A. Gaeta, C. Hernández-García, L. Plaja, A. Becker, A. Jaron-Becker, M. M. Murnane, H. C. Kapteyn, Bright coherent ultrahigh harmonics in the keV x-ray regime from mid-infrared femtosecond lasers. *Science* **336**, 1287–1291 (2012). doi:10.1126/science.1218497 Medline

44. T. Fan, P. Grychtol, R. Knut, C. Hernández-García, D. D. Hickstein, D. Zusin, C. Gentry, F. J. Dollar, C. A. Mancuso, C. W. Hogle, O. Kfir, D. Legut, K. Carva, J. L. Ellis, K. M. Dorney, C. Chen, O. G. Shpyrko, E. E. Fullerton, O. Cohen, P. M. Oppeneer, D. B. Milošević, A. Becker, A. A. Jaroń-Becker, T. Popmintchev, M. M. Murnane, H. C. Kapteyn, Bright circularly polarized soft X-ray high harmonics for X-ray magnetic

circular dichroism. *Proc. Natl. Acad. Sci. U.S.A.* **112**, 14206–14211 (2015). doi:10.1073/pnas.1519666112 Medline

45. P. M. Paul, E. S. Toma, P. Breger, G. Mullot, F. Augé, P. Balcou, H. G. Muller, P. Agostini, Observation of a train of attosecond pulses from high harmonic generation. *Science* **292**, 1689–1692 (2001). doi:10.1126/science.1059413 Medline

46. M. Hentschel, R. Kienberger, C. Spielmann, G. A. Reider, N. Milosevic, T. Brabec, P. Corkum, U. Heinzmann, M. Drescher, F. Krausz, Attosecond metrology. *Nature* **414**, 509–513 (2001). doi:10.1038/35107000 Medline

47. B. Rodenburg, M. P. J. Lavery, M. Malik, M. N. O'Sullivan, M. Mirhosseini, D. J. Robertson, M. Padgett, R. W. Boyd, Influence of atmospheric turbulence on states of light carrying orbital angular momentum. *Opt. Lett.* **37**, 3735–3737 (2012). doi:10.1364/OL.37.003735 Medline

48. C. Chen, Z. Tao, A. Carr, P. Matyba, T. Szilvási, S. Emmerich, M. Piecuch, M. Keller, D. Zusin, S. Eich, M. Rollinger, W. You, S. Mathias, U. Thumm, M. Mavrikakis, M. Aeschlimann, P. M. Oppeneer, H. Kapteyn, M. Murnane, Distinguishing attosecond electron-electron scattering and screening in transition metals. *Proc. Natl. Acad. Sci. U.S.A.* **114**, E5300–E5307 (2017). doi:10.1073/pnas.1706466114 Medline

49. P. Tengdin, W. You, C. Chen, X. Shi, D. Zusin, Y. Zhang, C. Gentry, A. Blonsky, M. Keller, P. M. Oppeneer, H. C. Kapteyn, Z. Tao, M. M. Murnane, Critical behavior within 20 fs drives the out-of-equilibrium laser-induced magnetic phase transition in nickel. *Sci. Adv.* **4**, eaap9744 (2018). doi:10.1126/sciadv.aap9744 Medline

50. A. Picón, A. Benseny, J. Mompart, J. R. Vázquez de Aldana, L. Plaja, G. F. Calvo, L. Roso, Transferring orbital and spin angular momenta of light to atoms. *New J. Phys.* **12**, 083053 (2010). doi:10.1088/1367-2630/12/8/083053

51. F. Calegari, A. Trabattoni, A. Palacios, D. Ayuso, M. C. Castrovilli, J. B. Greenwood, P. Decleva, F. Martín, M. Nisoli, Charge migration induced by attosecond pulses in bio-relevant molecules. *J. Phys. B At. Mol. Opt. Phys.* **49**, 142001 (2016). doi:10.1088/0953-4075/49/14/142001

52. G. Hermann, C.-M. Liu, J. Manz, B. Paulus, V. Pohl, J. C. Tremblay, Attosecond angular flux of partial charges on the carbon atoms of benzene in non-aromatic excited state. *Chem. Phys. Lett.* **683**, 553–558 (2017). doi:10.1016/j.cplett.2017.01.030

53. R. M. Kerber, J. M. Fitzgerald, S. S. Oh, D. E. Reiter, O. Hess, Orbital angular momentum dichroism in nanoantennas. *Commun. Phys.* **1**, 87 (2018). doi:10.1038/s42005-018-0088-2

54. See supplementary materials.

55. C. Hernández-García, J. A. Pérez-Hernández, J. Ramos, E. Conejero Jarque, L. Roso, L. Plaja, High-order harmonic propagation in gases within the discrete dipole approximation. *Phys. Rev. A* **82**, 033432 (2010). doi:10.1103/PhysRevA.82.033432

56. C. Hernández-García, A. Turpin, J. San Román, A. Picón, R. Drevinskas, A. Cerkauskaite, P. G. Kazansky, C. G. Durfee, Í. J. Sola, Extreme ultraviolet vector beams driven by infrared lasers. *Optica* **4**, 520 (2017). doi:10.1364/OPTICA.4.000520

57. M. Lewenstein, P. Balcou, M. Y. Ivanov, A. L'Huillier, P. B. Corkum, Theory of high-harmonic generation by low-frequency laser fields. *Phys. Rev. A* **49**, 2117–2132 (1994). doi:10.1103/PhysRevA.49.2117 Medline

58. A. Zaïr, M. Holler, A. Guandalini, F. Schapper, J. Biegert, L. Gallmann, U. Keller, A. S. Wyatt, A. Monmayrant, I. A. Walmsley, E. Cormier, T. Auguste, J. P. Caumes, P. Salières, Quantum path interferences in high-order harmonic generation. *Phys. Rev. Lett.* **100**, 143902 (2008). doi:10.1103/PhysRevLett.100.143902 Medline

59. M. V. Berry, Optical vortices evolving from helicoidal integer and fractional phase steps. *J. Opt. A, Pure Appl. Opt.* **6**, 259–268 (2004). doi:10.1088/1464-4258/6/2/018

60. J. Leach, E. Yao, M. Padgett, Observation of the vortex structure of non-integer vortex beam. *New J. Phys.* **6**, 71 (2004). doi:10.1088/1367-2630/6/1/071

61. S. N. Alperin, M. E. Siemens, Angular Momentum of Topologically Structured Darkness. *Phys. Rev. Lett.* **119**, 203902 (2017). doi:10.1103/PhysRevLett.119.203902 Medline

62. E. Karimi, L. Marrucci, C. de Lisio, E. Santamato, Time-division multiplexing of the orbital angular momentum of light. *Opt. Lett.* **37**, 127–129 (2012). doi:10.1364/OL.37.000127 Medline

63. I. J. Sola, E. Mével, L. Elouga, E. Constant, V. Strelkov, L. Poletto, P. Villoresi, E. Benedetti, J.-P. Caumes, S. Stagira, C. Vozzi, G. Sansone, M. Nisoli, Controlling attosecond electron dynamics by phase-stabilized polarization gating. *Nat. Phys.* **2**, 319–322 (2006). doi:10.1038/nphys281

64. H. Vincenti, F. Quéré, Attosecond lighthouses: How to use spatiotemporally coupled light fields to generate isolated attosecond pulses. *Phys. Rev. Lett.* **108**, 113904 (2012). doi:10.1103/PhysRevLett.108.113904 Medline

65. J. A. Wheeler, A. Borot, S. Monchocé, H. Vincenti, A. Ricci, A. Malvache, R. Lopez-Martens, F. Quéré, Attosecond lighthouses from plasma mirrors. *Nat. Photonics* **6**, 829–833 (2012). doi:10.1038/nphoton.2012.284

66. C. Hernández-García, A. Jaron-Becker, D. D. Hickstein, A. Becker, C. G. Durfee, High-order-harmonic generation driven by pulses with angular spatial chirp. *Phys. Rev. A (Coll. Park)* **93**, 023825 (2016). doi:10.1103/PhysRevA.93.023825

67. I. P. Christov, M. M. Murnane, H. C. Kapteyn, High-harmonic generation of attosecond pulses in the “single cycle” regime. *Phys. Rev. Lett.* **78**, 1251–1254 (1997). doi:10.1103/PhysRevLett.78.1251

68. M. Chini, K. Zhao, Z. Chang, The generation, characterization and applications of broadband isolated attosecond pulses. *Nat. Photonics* **8**, 178–186 (2014). doi:10.1038/nphoton.2013.362

69. W. Holgado, C. Hernández-García, B. Alonso, M. Miranda, F. Silva, L. Plaja, H. Crespo, I. J. Sola, Continuous spectra in high-harmonic generation driven by multicycle laser pulses. *Phys. Rev. A* **93**, 013816 (2016). doi:10.1103/PhysRevA.93.013816

70. J. Zhang, S.-J. Huang, F.-Q. Zhu, W. Shao, M.-S. Chen, Dimensional properties of Laguerre-Gaussian vortex beams. *Appl. Opt.* **56**, 3556–3561 (2017). doi:10.1364/AO.56.003556 Medline

71. Y. Esashi, C.-T. Liao, B. Wang, N. Brooks, K. M. Dorney, C. Hernández-García, H. Kapteyn, D. Adams, M. Murnane, Ptychographic amplitude and phase reconstruction of bichromatic vortex beams. *Opt. Express* **26**, 34007–34015 (2018). doi:10.1364/OE.26.034007 Medline

72. A. L’Huillier, P. Balcou, S. Candel, K. J. Schafer, K. C. Kulander, Calculations of high-order harmonic-generation processes in xenon at 1064 nm. *Phys. Rev. A* **46**, 2778–2790 (1992). doi:10.1103/PhysRevA.46.2778 Medline

73. G. Gbur, Fractional vortex Hilbert’s hotel. *Optica* **3**, 222–225 (2016). doi:10.1364/OPTICA.3.000222

74. S. Fu, S. Zhang, T. Wang, C. Gao, Pre-turbulence compensation of orbital angular momentum beams based on a probe and the Gerchberg-Saxton algorithm. *Opt. Lett.* **41**, 3185–3188 (2016). doi:10.1364/OL.41.003185 Medline

75. H. Chang, X.-L. Yin, X.-Z. Cui, Z.-C. Zhang, J.-X. Ma, G.-H. Wu, L.-J. Zhang, X.-J. Xin, Adaptive optics compensation of orbital angular momentum beams with a modified Gerchberg-Saxton-based phase retrieval algorithm. *Opt. Commun.* **405**, 271–275 (2017). doi:10.1016/j.optcom.2017.08.035

76. M. Seaberg, M. Donald, Nanoscale EUV Microscopy on a Tabletop: A General Transmission and Reflection Mode Microscope Based on Coherent Diffractive Imaging with High Harmonic Illumination. *Physics Graduate Theses & Dissertations* 6 (2014); https://scholar.colorado.edu/phys_gradetds/6

77. E. Karimi, G. Zito, B. Piccirillo, L. Marrucci, E. Santamato, Hypergeometric-Gaussian modes. *Opt. Lett.* **32**, 3053–3055 (2007). doi:10.1364/OL.32.003053 Medline

78. E. Yao, S. Franke-Arnold, J. Courtial, S. Barnett, M. Padgett, Fourier relationship between angular position and optical orbital angular momentum. *Opt. Express* **14**, 9071–9076 (2006). doi:10.1364/OE.14.009071 Medline

79. S. N. Alperin, R. D. Niederriter, J. T. Gopinath, M. E. Siemens, Quantitative measurement of the orbital angular momentum of light with a single, stationary lens. *Opt. Lett.* **41**, 5019–5022 (2016). doi:10.1364/OL.41.005019 Medline